Applied Catalysis B: Environmental 342 (2024) 123374

Contents lists available at ScienceDirect

Applied Catalysis B: Environmental

journal homepage: www.elsevier.com/locate/apcatb

# A multifunctional membrane based on $TiO_2$/PCN-224 heterojunction with synergistic photocatalytic-photothermal activity under visible-light irradiation

Zhongxi Lu [a,1], Jingsong Gao [a,1], Shaosheng Rao [a,1], Cheng Jin [a], Haopeng Jiang [a], Jun Shen [b,*], Xiaohui Yu [a], Weikang Wang [a], Lele Wang [a], Juan Yang [a,*], Qinqin Liu [a,*]

[a] School of Materials Science and Engineering, Jiangsu University, Zhenjiang 212013, Jiangsu, China
[b] School of Pharmacy, Suzhou Vocational Health College, Suzhou 215009, Jiangsu, China

ARTICLE INFO

*Keywords:*
Multifunctional membrane
$TiO_2$
PCN-224
Synergistic photocatalytic-photothermal contribution

ABSTRACT

Photocatalysis is widely recognized as a promising method for various clean applications, and membrane technology is emerging as a potential functional form of photocatalysts. In this paper, an organic–inorganic $TiO_2$/PCN-224 (TP) core-shell hybrid was fabricated and loaded on a PVDF membrane using vacuum filtration technique. This integration enabled the creation of a multifunctional TP-constructed-membrane with synergistic photocatalytic-photothermal activity for $H_2$ generation, tetracycline (TC) degradation and inactivation of Staphylococcus aureus (*S. aureus*). The high efficiency of the TP membrane under visible light can be attributed to the photothermal and photodynamic effects induced by PCN-224, as well as the role of $TiO_2$ as the electron transfer platform. Moreover, the superhydrophilicity of the TP membrane facilitated enhanced rates of water-based catalytic reactions. As a result, under visible light, the optimal TP membrane demonstrated remarkable outcomes under visible light, including $H_2$ generation at a rate of 1.88 mmol $g^{-1}$ $h^{-1}$, 86% degradation of TC (at a concentration of 50 mg/L) and 99.99% inactivation of *S. aureus*. These results exemplify the achievement of multiple objectives with a single catalyst, truly embodying the concept of "three birds, one stone".

## 1. Introduction

Nowadays, the rapid development of industrialization has led to various issues for both human beings and the earth, especially, energy shortage and water pollution [1–3]. For example, the misuse of antibiotics in the modern medicine not only contaminates water but also contributes to the emergence of drug-resistant bacteria [4–6]. In view of these phenomena, green technologies that can produce clean energy for industry, treat environmental pollution and cure human diseases have become hot topics in scientific research [7,8]. Since the initial discovery of photocatalysis in 1972 [9], numerous green applications have been explored, including water splitting for $H_2$ generation [10,11], antibiotic degradation [12,13], inactivation of drug-resistant bacteria [14,15], $CO_2$ reduction [16,17]. Considerable progress has been made in these areas. As one of the earliest studied semiconductors, $TiO_2$ with a wide band gap (3.2 eV) demonstrates excellent redox properties necessary for driving various redox reactions and is proficient in generating reactive oxygen species (ROS), making it a versatile semiconductor [18,19]. For example, Wang et al. prepared Ti and O vacancy modified $TiO_2$, which produced $O_2^-$ and·OH for achieving the degradation of ofloxacin and the reduction of Cr(VI) [20]. Stylianou et al. reported the synthesis of a nitrogen and sulfur-doped $TiO_2$ photocatalyst capable of full-spectrum $H_2$ production and herbicide degradation [21]. However, pure $TiO_2$ is often faces limitations due to fast carrier recombination and light absorption capacity [22–24].

In order to address the plight of $TiO_2$, construction of heterojunctions with other semiconductor that have strong light response, particularly photothermal effect, can broaden the light absorption and promote the production of carriers to enhance the photocatalytic activity [25,26]. Organic semiconductors with narrow bandgaps unfold a wide light utilization, and combining them with inorganic semiconductors like $TiO_2$ to form inorganic-organic photocatalysts is a promising design concept to take the advantage of their merit fully [27,28]. Among the reported organic semiconductors, metal-organic frameworks (MOFs),

* Corresponding authors.
*E-mail addresses:* shenjun@szhct.edu.cn (J. Shen), yangjuan6347@ujs.edu.cn (J. Yang), qqliu@ujs.edu.cn (Q. Liu).
[1] These authors contributed equally.

https://doi.org/10.1016/j.apcatb.2023.123374
Received 28 July 2023; Received in revised form 16 September 2023; Accepted 6 October 2023
Available online 7 October 2023

composed of metal clusters and organic ligands, demonstrate big specific surface area, multiple porosity, and adjustable bandgap [29]. In MOFs, the bridging ligands function as antennas to adsorb light and convert the light energy into carriers, and porphyrin as bridging ligand is effective for capturing visible light [30]. PCN-224, a typical MOF consisting of porphyrin as the ligand and Zr as the metal center, has high structural stability and can generate ROS under light of 420 ~ 650 nm [31]. Jiang et al. used PCN-224 for photodynamic therapy (PDT) of chronic wounds infected by multidrug-resistant bacteria [32]. Wei et al. deposited Ag nanoparticles on PCN-224, which produced a large amount of $^1O_2$ under light irradiation and realized the inactivation of bacteria [33]. Besides that, PCN-224 has also been reported as a photothermal agent, demonstrating high sterilization performance for drug-resistant bacteria [34]. The photothermal effect converts the photon energy into heat, elevating the local temperature of the catalyst to facilitate the activation of the reactant molecules and promoting the charge transfer to enhance the efficiency of photocatalysis [35]. Coupling the PCN-224 with $TiO_2$ holds promise for creating an efficient organic–inorganic $TiO_2$/PCN-224 hybrid with diverse functionality. However, it is noted that photocatalysts are in powder-form which is not suitable for real application [36]. Integrating powder photocatalysts onto substrates is promising offers a promising solution, as it allows for easy recycling [37]. Recently, Yan et al. deposited g-$C_3N_4$ onto polyvinylidene fluoride (PVDF) membrane to obtain a composite membrane with high hydrophilicity and plentiful transport channels, achieving eminent photocatalytic degradation and antibacterial efficiency; this membrane maintained stability over 35 consecutive recycling cycles [38].

Herein, we aimed to combine the benefits of membrane technology with photocatalysis. Firstly, $TiO_2$ nanosheets were prepared and then coupled with PCN-224 to construct the organic–inorganic $TiO_2$/PCN-224 hybrid powders, followed by coating onto a PVDF membrane via vacuum filtration method to prepare a self-supported membrane with synergistic photocatalytic-photothermal activity. A similar Type-II electron transfer mode was supposed for the $TiO_2$/PCN-224 hybrid, foreshadowing of the carrier separation under visible light. The wide light absorption ability and photothermal effect of PCN-224 contributed to the visible light performance of the $TiO_2$/PCN-224 membrane. Besides that, we investigated multiple applications, including $H_2$ generation, antibiotic degradation and antibacterial inactivation, to demonstrate the versatility of the $TiO_2$/PCN-224 membrane and maximize the potential benefits of the membrane. This work serves as a foundation for future research in constructing multifunctional membranes to expand the application of photocatalysis.

## 2. Experimental section

### 2.1. Synthesis of PCN-224 photocatalysts

The synthesis method of square PCN-224 is similar to previous report [39]. Initially, a beaker was filled with 15 ml N, N-dimethylformamide (DMF). Then, 0.05 g of tetrakis (4-carboxyphenyl)-porphyrin (TCPP) and 0.078 g of $ZrCl_4$ were added to the DMF, and the mixture was stirred for 15 min, then, 5.4 g of benzoic acid (BA) was added to the solution, and stirring was continued until the solution turned green. The resulting solution was hydrothermal treated at 120 ℃ for 48 h. After the treatment, the samples were collected, washed 3 times with methanol and acetone and dried at 60 ℃. The yield of the synthesis process was 78%.

### 2.2. Synthesis of $TiO_2$ and $TiO_2$/PCN-224 photocatalysts

$TiO_2$ nanosheets were synthesized according to the method reported earlier [14]. $TiO_2$/PCN-224–20 (TP-20) was prepared by a simple one-step solvent mixing method. 0.1 g $TiO_2$ nanosheets were added into a beaker containing 30 ml DMF and ultrasounded for 30 min. A certain amount of PCN-224 (11, 25, 43 mg) was added to the solution and stirred for 5 h. The precipitation was collected, centrifuged, and dried at 60 ℃ overnight to form TP-10, TP-20 and TP-30 samples. The preparation process of the composite is unfolded in Fig. 1.

### 2.3. Synthesis of photocatalyst coupled PVDF membrane

The prepared catalysts were deposited on the surface of PVDF membrane by pumping and filtering technology to form $TiO_2$/PVDF, PCN-224/PVDF, TP-10/PVDF, TP-20/PVDF, and TP-30/PVDF membranes.

### 2.4. Photocatalytic $H_2$ generation experiment

The prepared membranes loaded with 25 mg photocatalysts were put into a reaction vessel, and then 8 ml TEOA and 72 ml $H_2O$ were added, and then the vessel was injected with $N_2$ to remove the air. Xenon lamp (300 W) or LED light was used to induce the catalytic reaction. The produced $H_2$ was extracted from the reactor and then tested by a gas chromatograph (GC-2014, Shimazu Corporation, Japan).

### 2.5. Adsorption and photodegradation towards TC

The prepared membranes loaded with 5 mg photocatalysts were placed in TC solution (50 mg/L, 50 ml). In order to ensure the saturation adsorption of TC, adsorption was carried out in the dark for 60 min 300 W Xenon lamp with AM 1.5 G filter or 420 nm cut-off filter was used as the reaction light source. In the photocatalytic degradation process, 3 ml reaction suspension was extracted and centrifuged to collect the clear liquid for detection of residual TC concentration at 357 nm by ultraviolet spectrophotometer.

### 2.6. Photocatalytic antibacterial experiment

*S. aureus* were used as targets for photocatalytic bactericidal experiments. In general, the diluted bacterial solution was added to a test tube containing PBS buffer solution, membranes were added and irradiated (Xe lamp) in bath shaker at 37 ℃. After the end of the catalytic process, 10 μL suspended liquid was taken out and diluted and held in a 37 ℃ oven for 24 h to calculate the colony forming unit (CFU). Sample characterization, and preliminary preparation before the antibacterial experiment were supplemented in the Supplementary Material.

## 3. Results and discussion

### 3.1. Characterization of photocatalysts

$TiO_2$, PCN-224 and TP were analyzed by the scanning electron microscopy (SEM), transmission electron microscopy (TEM). $TiO_2$ demonstrates nanosheet morphology with a size of approximately 150 nm (Fig. 2a and d). The PCN-224 appears as a cube morpholoy, varying in size from 3 to 5 μm (Fig. 2b). When $TiO_2$ is combined with PCN-224, the $TiO_2$ nanosheets tightly wrap around the surface of the cubic PCN-224, forming a core-shell $TiO_2$/PCN-224 hybrid (Fig. 2c, e, f). According to the element mapping of TP-20 in Fig. 2g, h, i, j, k, Zr, O and C elements display similar cubic morphology and the Ti element is observed to clad over the Zr element, confirming that the $TiO_2$ nanosheets are evenly distributed on the surface of PCN-224 to form a core-shell structure in the $TiO_2$/PCN-224 hybrid. The intimate interface of this core-shell structure is favorable for electron transfer.

The crystal structures of PCN-224, $TiO_2$ and TP composites were characterized by powder X-ray diffraction (XRD). The PCN-224 has obvious characteristic diffraction peaks at 4.6°, 6.4°, 7.9°, 9.1°, 11.2° and 13.7°, corresponding to the (002), (022), (222), (004), (224), (006) crystal faces of PCN-224, respectively (Fig. 3a) [39]. The characteristic peaks of the $TiO_2$ nanosheets correspond to (101), (004), (200), (105), (211), (204), (220), (215) and (301) crystal faces of anatase $TiO_2$ (JCPDS 21–1272), respectively (Fig. 3b) [40]. For the TP composite, in

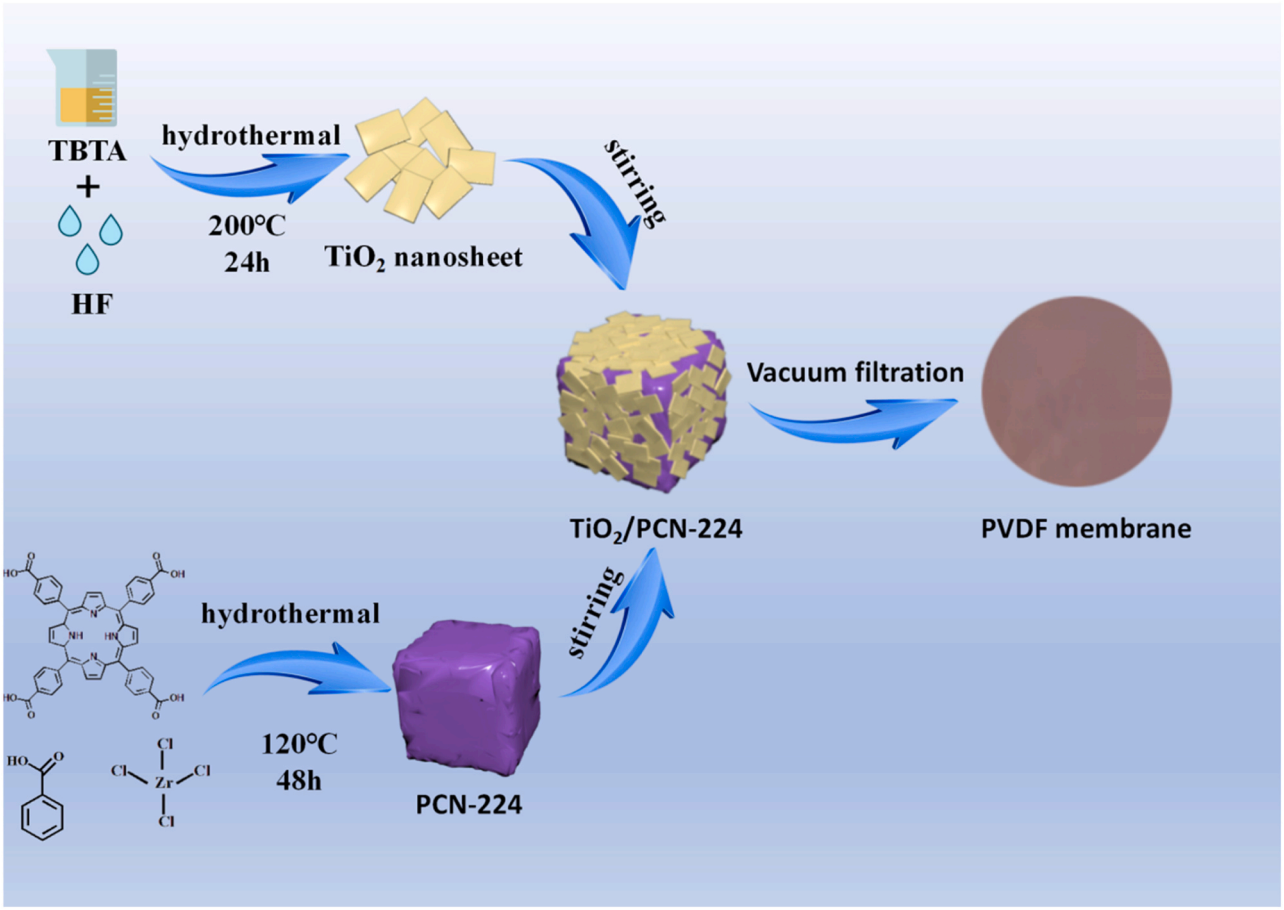


**Fig. 1.** Schematic illustration of preparation process of $TiO_2$/PCN-224 membrane.

general, the $TiO_2$ and PCN-224 still maintain their corresponding crystal structure. The $TiO_2$ is the dominant component in the composite (Fig. 3b), and the peak intensity of the PCN-224 becomes more and more obvious with the gradual increase in the amount of PCN-224 (Fig. 3C).

Moreover, Fourier transform infrared spectrometry (FT-IR) and X-ray photoelectron spectroscopy (XPS) were used to verify the chemical status of the prepared catalysts. The peak at 3421 $cm^{-1}$ is attributed to the O-H group (Fig. 3d) [33], PCN-224 has two asymmetric stretching peaks at 1650 and 1264 $cm^{-1}$, respectively, which are attributed to the C═O and C-OH functional groups in $H_2TCPP$ [33]. $TiO_2$ has two peaks at 1634 and 1387 $cm^{-1}$, which are attributed to the O-H group and the Ti-O-Ti group, respectively. The observation of vibration peak belonging to the $H_2TCPP$ in the TP-20 indicates the successful combination of the $TiO_2$ and PCN-224.

The Ti, O, N, C, and Zr coexist in the survey spectrum of the TP-20 (Fig. 3e). For the Ti spectrum of $TiO_2$, two peaks belonging to the 2p1/2 and 2p3/2 orbitals of Ti are observed at 464.6 and 458.8 eV [14], respectively, and both peaks are slightly offset in the TP-20 (Fig. 3f). The PCN-224 has two characteristic peaks at 185.4 and 183 eV, corresponding to 3d3/2 and 3d5/2 orbitals respectively, indicating the presence of $Zr^{4+}$ ions in PCN-224 (Fig. 3g) [39]. The N1s orbit of the PCN-224 are located at 400.3, 399.5 and 397.6 eV, respectively [39,41]. The Zr and N peaks belonging to the PCN-224 are also observed in the TP-20, indicating that coupling of the $TiO_2$ does not affect the coordination of Zr and N in the PCN-224. The TP-20 represents -$N^+$H- in the porphyrin group, while the 400.2 and 399.1 eV peaks represent -NH- and =N-, respectively. Two peaks are observed at 531.99 and 530.06 eV in the O 1 s orbital of the $TiO_2$, corresponding to the O-H bond and Ti-O bond, respectively [14]. Three peaks appear in the O 1 S spectrum of the PCN-224, which are located at 533.2, 531.91 and 530.47 eV, corresponding to O-H, C═O and Zr-O-Zr groups respectively [14,39]. For the composite, the peak at 529.79 eV corresponds to Ti-O in $TiO_2$ and the peak at 530.93 eV corresponds to C═O in PCN-224 [14,39,41], fully proving the successful combination of $TiO_2$ and PCN-224 of the TP composite.

The surface structure and cross section morphology of the TP-20 membrane are presented in Fig. 4a and b, the TP hybrids are adhered to the PVDF film, forming a porous film with thickness of about 200 μm. Notably, no angle between the water droplets and TP-20/PVDF film is captured, indicating a contact angle of of 0° (Fig. 4c and d), which is smaller than that of bare PVDF membrane (13.6°).

The superhydrophilicity of the TP-20/PVDF film is a very powerful factor in the photocatalytic reaction process in water. The photothermal activity of the PVDF, $TiO_2$/PVDF, PCN-224/PVDF and TP-20/PVDF film is recorded (Fig. 4e and f) for 20 min under simulated sunlight irradiation (the room temperature during the test was 29.3 ℃). The PVDF and $TiO_2$/PVDF reach 32.8 and 38.8 ℃, respectively. The temperature of PCN-224/PVDF reaches 54.3 ℃ due to the strong photothermal conversion ability of the ligand porphyrins in PCN-224 structure. Following the incorporation of PCN-224, the TP-20/PVDF film experiences an increase in temperature. Specifically, the temperature of the TP-20/PVDF film reaches 45.6 ℃ after 2 min and 51 ℃ after 20 min. After turning off the light, a fast-cooling process is observed. The photothermal effect produced by the TP-20 promotes various catalytic processes, including the degradation, sterilization, and $H_2$ production. In detail, under light irradiation, the PCN-224 generates electrons that migrate to $TiO_2$, thereby enhancing the catalytic reaction. Additionally, the high surface temperature of the catalyst contributes to accelerated reaction kinetics. The efficiency of photothermal conversion of the TP-20 under LED Lamp of 420 nm was calculated to be 17.3% [42]. The TP-20/PVDF film still

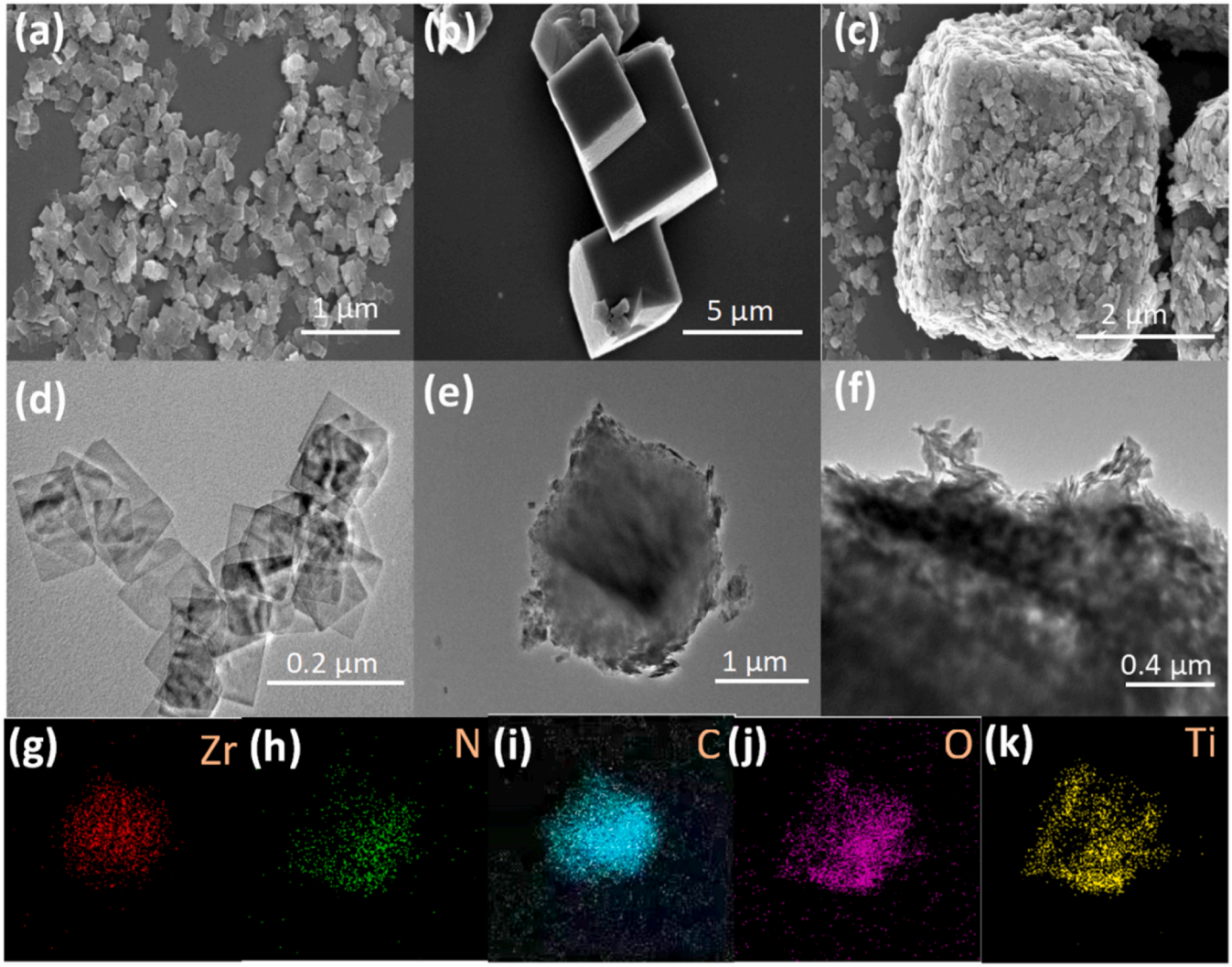


**Fig. 2.** SEM images of (a) $TiO_2$, (b) PCN-224, (c) TP-20; TEM images of (d) $TiO_2$, (e-f) TP-20; (g-k) corresponding elemental mappings showing the distribution of C, N, Zr, O and Ti in TP-20 hybrid.

exhibits stable photothermal performance throughout four cycles (Fig. 4g), further affirming its potential for reuse.

### 3.2. Evaluation of photocatalytic activity

Under the irradiation of 300 W Xe lamp, $TiO_2$ and PCN-224 display low photocatalytic $H_2$ generation with rate of 6 μmol $g^{-1}$ $h^{-1}$ and 69.4 μmol $g^{-1}$ $h^{-1}$ (Fig. 5a). The composites demonstrate much higher $H_2$ generation than that of the bare samples, when the addition amount of the PCN-224 reaches 20 wt%, the $H_2$ evolution of the TP-20 reaches 590.30 μmol $g^{-1}$ $h^{-1}$, which is 98 and 9 times higher than that of $TiO_2$ and PCN-224, respectively (Fig. 5b).

The $H_2$ generation test was also carried out under LED lamp with $\lambda = 365$, 420 and 500 nm, respectively. Under the light of 365 nm, the TP-20 shows excellent $H_2$ generation (~ 3.39 mmol $g^{-1}$ $h^{-1}$), which is about 34 times higher than $TiO_2$ (~ 0.10 mmol $g^{-1}$ $h^{-1}$) (Fig. 5c). However, under the light of 420 nm, $TiO_2$ demonstrates no activity and the PCN-224 and TP-20 still shows $H_2$ generation of 0.32 and 1.88 mmol $g^{-1}$ $h^{-1}$, respectively, indicating that the PCN-224 is the main functional semiconductor that accounts for the photocatalytic performance. Interestingly, the TP-20 has a $H_2$ generation rate of 0.12 mmol $g^{-1}$ $h^{-1}$ at 500 nm light excitation. In summary, without the assistance of any co-catalyst, the $H_2$ evolution activity of the TP-20 is very impressive, far exceeding the performance of the reported $TiO_2$-based catalysts (Table S1, Fig. 5g), and the TP-20 demonstrates $H_2$ generation activity under visible light while no activity is observed for bare $TiO_2$.

The photocatalytic degradation activity in water was also analyzed using tetracycline (TC) as the target. Under 1 h dark adsorption, the $TiO_2$ adsorbs nearly 11% of TC. Due to the large specific surface and pore structure of MOF, the PCN-224 has good adsorption performance with adsorption TC content of 36%. The TC adsorption of the TP-20 is about 13%, lower than of the PCN-224, which is maybe due to that $TiO_2$ nanosheets pack over the cubic PCN-224 in the TP-20 composite (Fig. 5d). Under the light of Xe lamp with an AM 1.5 filter, the TP-20 degrades nearly 83% of TC (50 mg/L) under 90 min illumination, which is much higher than the $TiO_2$ (66%) and PCN-224 (45%) (Fig. 5d). Fig. 5e shows the curves of $-\ln(C_t/C_0)$ of the $TiO_2$, PCN-224 and TP-20, and the linear fit indicates the TC degradation conforms to the quasi-first-order kinetic equation. The constant rate ($K$) of TC degradation is also calculated. and shown in Fig. 5f, the order of the $K$ is: TP-20 > $TiO_2$ > PCN-224 > PVDF. The degradation rate of the TP-20 is 0.033 $min^{-1}$, which is 1.8 and 2.1 times higher than that of $TiO_2$ (0.018 $min^{-1}$) and PCN-224 (0.015 $min^{-1}$), respectively. The degradation performance of the TP-20 was also tested by using different dosage of catalysts and different concentrations of TC as the target. As illustrated in Fig. S1 when the addition amount of the TP-20 is 2.5 mg, nearly 77% of TC can be degraded within 90 min and the corresponding degradation rate is

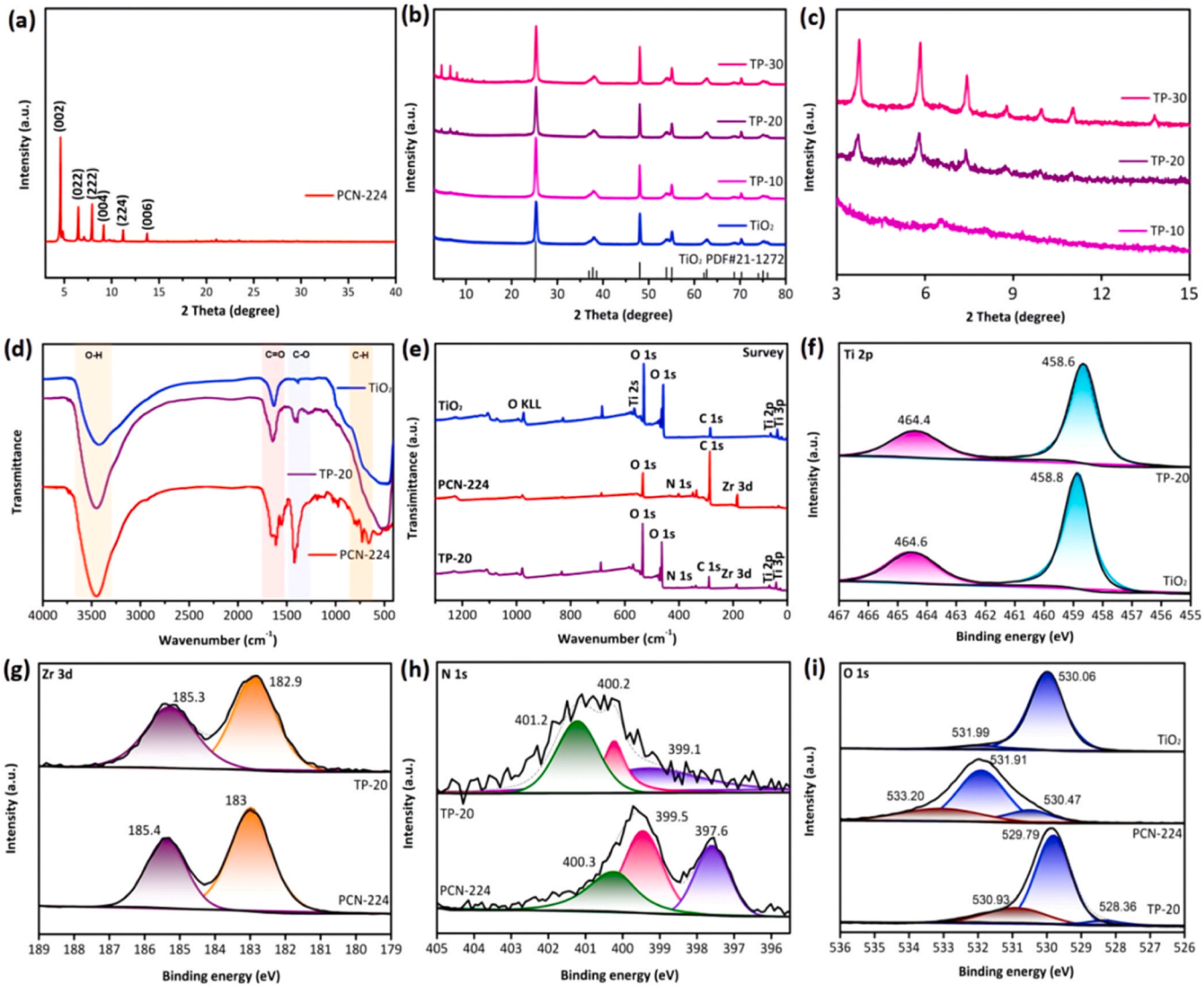


**Fig. 3.** XRD patterns of (a) PCN-224, (b and c) $TiO_2$ and TP hybrid; (d) FT-IR and (e) XPS analysis of $TiO_2$, PCN-224, TP-20 (f-i) high-resolution XPS spectra of Ti 2 p, Zr 3 d, N 1 s, O 1 s, respectively.

0.015 $min^{-1}$. When the amount of the TP-20 is increased to 5 mg, the rate reaches 0.033 $min^{-1}$, and further increasing the amount can not enhance the degradation rate. The concentration of TC is fixed at 25 mg/L (Fig. S2), the degradation rate of the TP-20 is 0.0535 $min^{-1}$, far exceeding the degradation activity of most recently reported $TiO_2$-based and PCN-224-based photocatalytic materials (Table S2, Fig. 5h). With the gradual increase of TC concentration, the degradation rate declines. When the TC concentration reaches 100 mg/L, the TP-20 still can degrade 60% of TC within 90 min, and the degradation rate reaches 0.01 $min^{-1}$ (Fig. S3). The photodegradation of TC by TP-20 under visible light was tested. Excluding the influence of adsorption factors, the results show $TiO_2$ presents almost no photocatalytic degradation activity, while PCN-224 degrades nearly 76%, while TP-20 still unfolds the best degradation activity, degrading nearly 86% of TC (Fig. S4). In addition, we also tested the photocatalytic degradation activity of different antibiotics against the TP-20. At the same catalytic dose (5 mg) and antibiotic concentration (50 mg/L) as previously tested conditions, the TP-20 degrades nearly 81% of oxytetracycline and 92% of ofloxacin, respectively, within 60 mins (Fig. S5).

The photocatalytic antibacterial activities of $TiO_2$ and TP-20 were analyzed using *Staphylococcus aureus* (*S.aureus*) as target to further explore their potential applications in wastewater treatment. First, the toxicity of $TiO_2$ and TP-20 catalysts against *S.aureus* was evaluated under dark conditions. Under dark condition, $TiO_2$ and TP-20 demonstrates no inhibition on the survival of *S.aureus*, which proves their good biocompatibility (Fig. 6a). Xe lamp with an AM 1.5 filter is used, and when the *S.aureus* is exposed to light for 90 min without any photocatalyst, no significant colony reduction is observed, indicating that light has little inhibitory effect on bacterial survival. The catalyst concentration of the $TiO_2$ and TP-20 is 200 ppm. For $TiO_2$, after 45 min irradiation, the number of colonies changes from $6.13 \times 10^7$ CFU $ml^{-1}$ to $3.92 \times 10^7$ CFU $ml^{-1}$ (Fig. 6b), and the bactericidal efficiency reaches 36.76% (Fig. 6c). The number of colonies of the TP-20 changes from $6.04 \times 10^7$ CFU $ml^{-1}$ to $0.15 \times 10^7$ CFU $ml^{-1}$ after irradiation (Fig. 6b), and the bactericidal efficiency reaches 97.54% (Fig. 6c) after 45 min. With the time extends to 90 min, TP-20 kills nearly 99.99% of *S.aureus*. The photocatalytic bactericidal activities of the TP-10, TP-20 and TP-30 is also compared in Fig. S6, the TP-10 and TP-30 kills nearly 87.56% and 96.32% of *S.aureus*, respectively, and the TP-20 demonstrates the best antibacterial activity (Fig. S7). The bactericidal activity of $TiO_2$ and TP-20 under visible light was also tested. As shown in Fig. 6d, after 60 min of irradiation, $TiO_2$ had almost no bactericidal activity under visible light, and the number of colonies changes from $6.12 \times 10^7$ to $6.09 \times 10^7$ CFU $ml^{-1}$. The TP-20 has excellent bactericidal activity with

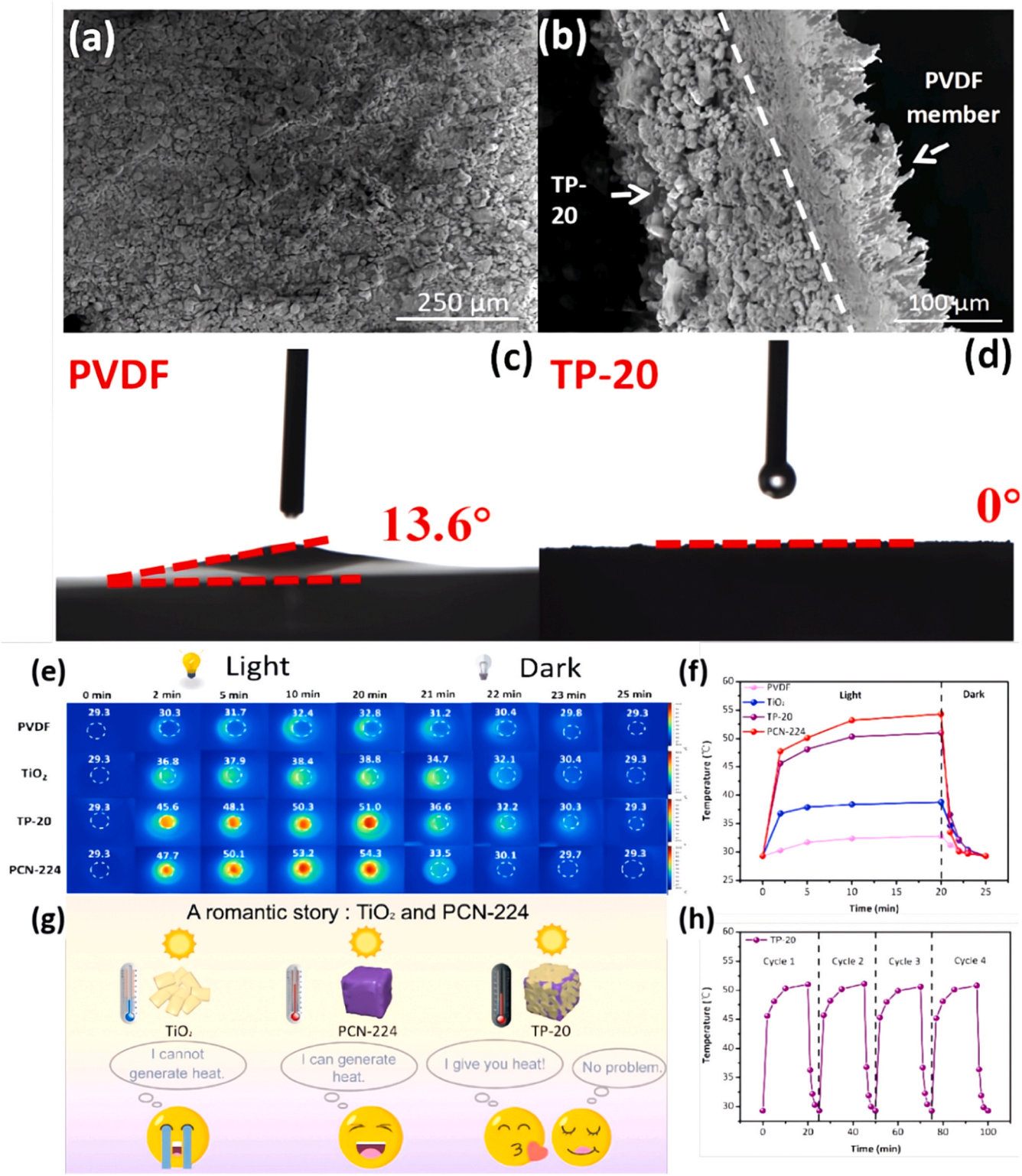


**Fig. 4.** SEM images of (a) surface and (b) cross-section of TP-20 membrane; (c) water contact angle of (d) PVDF and TP-20 membrane. (e) Thermal images and (f) thermal curves of different samples; (g) photothermal mechanism and (h) heating cycle of the TP-20 membrane.

bactericidal efficiency of 86.53% under visible light, and the number of colonies changes from $6.12 \times 10^7$ to $0.83 \times 10^7$ CFU $ml^{-1}$. With the time extends to 120 min, the inactivation of *S. aureus* of the TP-20 is nearly 99.99%.

To further validate its stability, the bactericidal performance of the TP-20 is also evaluated over five consecutive times. The TP-20 still manifests good bactericidal efficiency after four cycles (Figs. S8 and S9). The same XRD pattern of the TP-20 confirms the unchanged structure and stability of the TP-20 (Fig. S10). In addition, as presented in Figs. S11 and S12, the effect of different amount of the TP-20 catalyst (50, 100, 200, and 300 ppm) on the inactivation efficiency of *S. aureus* under simulated sunlight was tested. The results indicate that as the

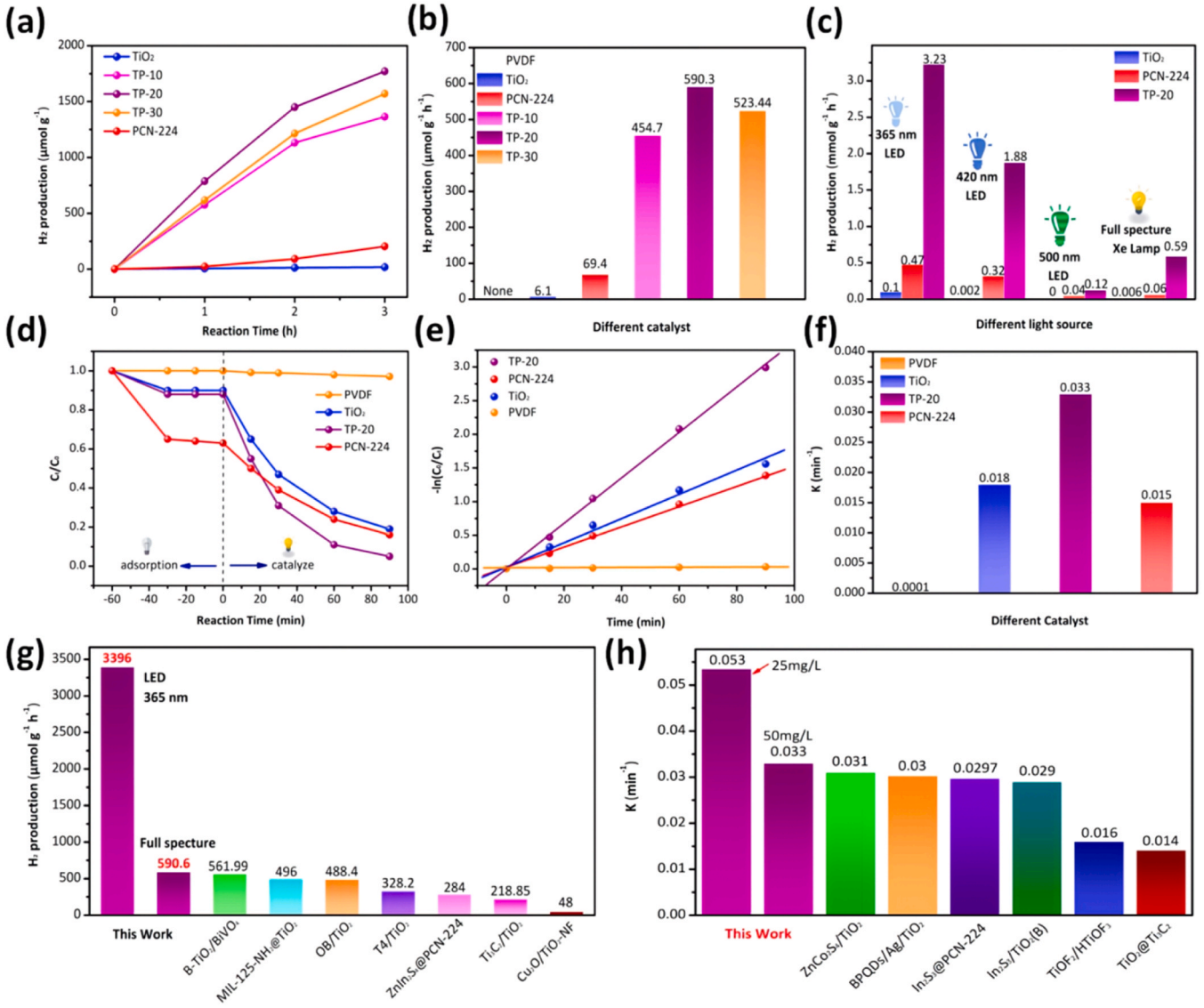


**Fig. 5.** (a) $H_2$ generation and (b) $H_2$ generation rates of $TiO_2$, PCN-224, TP-10, TP-20, TP-30; (c) photocatalytic $H_2$ evolution rate of $TiO_2$, TP-20 at 365, 420, 500 nm and full spectrum; (d) TC degradation performance, (e) degradation curves, (f) degradation rate constants of $TiO_2$, PCN-224, TP-20; (g and h) comparison of photocatalytic properties between the TP-20 and literatures [26,39,41,43–52].

catalyst concentration increases, the inactivation ability of TP-20 enhances. To ascertain the synergistic effect of the photocatalytic and photothermal effect, the *S. aureu* inactivation by the TP-20 was tested at 50 ℃ (without light) and 0 ℃ (under simulated sunlight), respectively, eliminating the function of light or temperature. It can be found from Figs. S13 and S14 that the inactivation rate at 50 ℃ (without light) is 8.53%, whereas the TP-20 can eradicate nearly 82.45% of *S. aureu* at 0 ℃ (under simulated sunlight). This verifies that the ROS generated by the photocatalytic process primarily contributes to bacterial death, while the photothermal effect further enhances sterilization efficiency. SEM images capture the physical change of bacterial morphology before and after the photocatalytic process. *S. aureus* appears a spherical shape under survival conditions, and the cell wall is damaged upon light irradiation (Figs. S15 and S16). To demonstrate the potential real-world application of TP-20, bactericidal experiments were also carried out under the natural sunlight, the TP-20 achieves a bactericidal efficiency of 96.53% and 99.99% after 45 min and 90 min, respectively (Fig. 7a and b).

### 3.3. Photocatalytic mechanism

The charge separation behavior of the $TiO_2$, PCN-224 and TP-20 was investigated by transient photocurrent (PC) response and electrochemical impedance spectroscopy (EIS). Under Xe lamp irradiation, the TP-20 manifests higher PC than that of $TiO_2$ and PCN-224 (Fig. S17). Under 420 nm light (Fig. S18), $TiO_2$ exhibits minimal intensity, suggesting that $TiO_2$ has no obvious photogenerated carrier migration under visible light. This is because $TiO_2$ can only be excited by the UV-light. However, both TP-20 and PCN-224 demonstrate light response, with TP-20 exhibiting a higher light response compared to PCN-224, indicating that the TP-20 possesses enhanced photogenerated carrier migration ability. Similarly, the EIS semicircle radius of TP-20 is the smallest among the samples, signifying that the least resistance of the interface for the TP-20 (Fig. S19). In addition, transient fluorescence spectroscopy (TRPL) was used to analyze the photogenerative carrier lifetimes of the $TiO_2$ and PCN-224. As shown in Fig. S20, the TP-20 has a lower photogenerated carrier lifetime, indicating that a faster carrier transfer channel in TP-20 compared to that of $TiO_2$. Based on the preceding results, the TP-20 has a faster photogenerated carrier migration

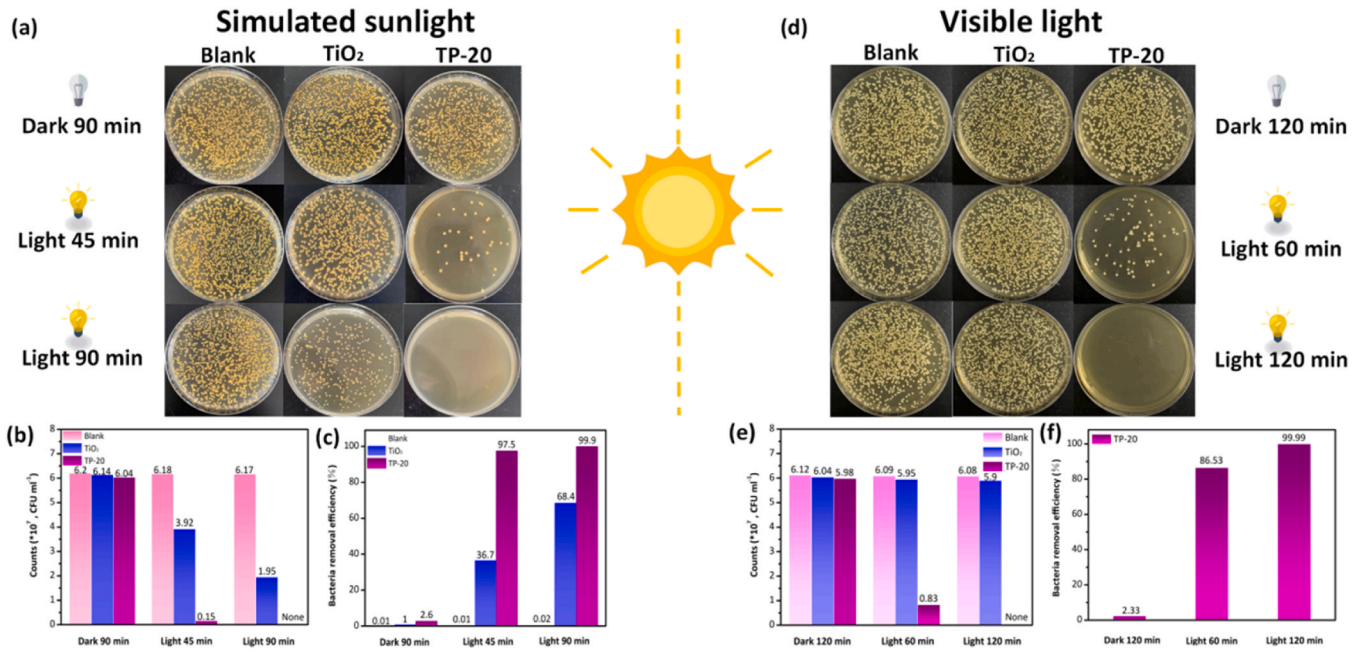


**Fig. 6.** (a) Antibacterial experiments, (b) colony statistics and (c) bactericidal efficiency of $TiO_2$ and TP-20 under dark and Xe light. (d) Antibacterial experiments (e), colony statistics, (f) bactericidal efficiency of $TiO_2$ and TP-20 under dark and visible light.

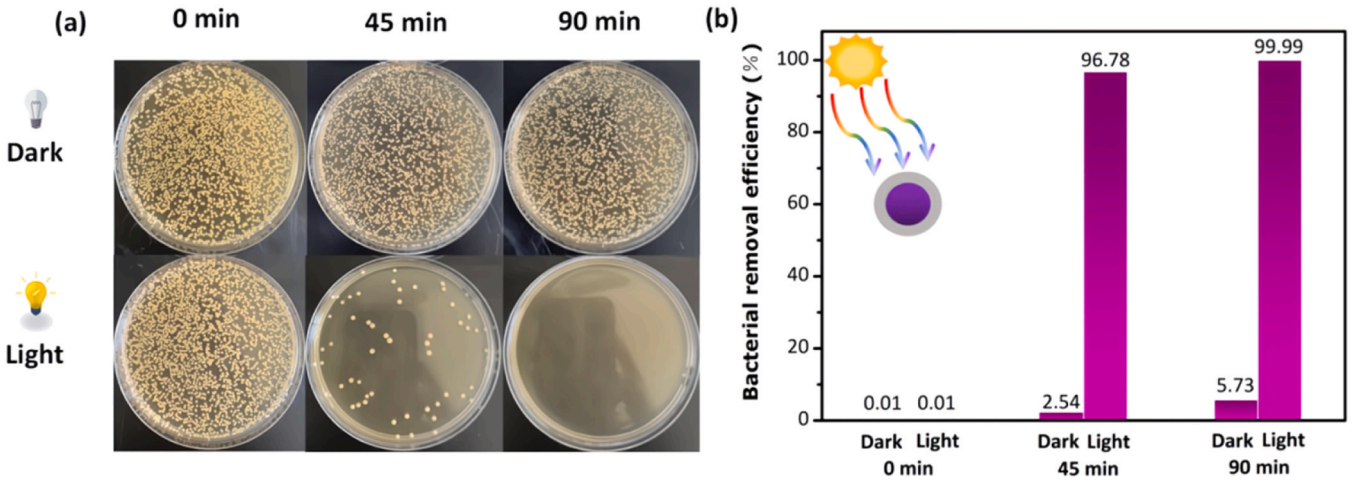


**Fig. 7.** (a and b) Photocatalytic bactericidal properties of TP-20 under real sunlight.

rate, which is more favorable for photocatalytic reaction.

The light absorption capacity of $TiO_2$, PCN-224 and TP photocatalysts was measured by UV–vis DRS. The optical absorption of $TiO_2$ is limited to less than 400 nm (Fig. 8a), while PCN-224 has a wide optical absorption range (~ 900 nm). The composite illustrates a wide light absorption range (~ 800 nm) due to the coupling of the PCN-224. Fig. 8b presents the Tauc diagram of $TiO_2$ and PCN-224, and the band gap of $TiO_2$ and PCN-224 is 3.2 and 1.7 eV, respectively [14,39]. According to the Mott-Schottky curve slope diagram of $TiO_2$ and PCN-224 (Figs. S21 and S22), both $TiO_2$ and PCN-224 are n-type semiconductors. On the ground of $E_{fb}=E_{Ag/AgCl}+ 0.059\ pH + E^0_{Ag/AgCl}$ (electrolyte pH is 6.8, $E^0_{Ag/AgCl}$ is 0.197 eV) [53], the flat potential of PCN-224 and $TiO_2$ is − 0.65 V and − 0.83 V, respectively. The conduction bands (CB) of PCN-224 and $TiO_2$ (ECB vs. NHE, pH=0) are − 0.34 and − 0.53 V, respectively [14,41]. Based on the equation of $E_{VB}=E_{CB}+Eg$, the valence band (VB) positions of $TiO_2$ and PCN-224 are 2.63 V and 1.41 V, respectively.

The functional radicals of the TP-20 during the photocatalytic process under light irradiation is investigated. The semiconductor can produce photogenerated electrons and holes, which react with $H_2O$ or $O_2$ to generate ROS, such as hydroxyl free radicals (·OH), superoxide free radicals ($O_2^-$) and singlet oxygen ($^1O_2$). To investigate the functional ROS of the TP-20, the electron paramagnetic resonance (EPR) characterization and ROS capturing experiment were carried out. The $TiO_2$, PCN-224 and TP-20 are found to generate $O_2^-$ and·OH radicals after 5 min of simulated sunlight irradiation, and the TP-20 can produce more $O_2^-$ and·OH radicals compared to that of the $TiO_2$ and PCN-224 (Fig. 8d, e, and f). Interestingly, the VB potential of PCN-224 does not satisfy the conversion requirements for $OH^-$/·OH (2.38 V), suggesting that·OH does not come from $OH^-$. To address this uncertainty, a more in-depth investigation is conducted. The production of $H_2O_2$ were tested over the PCN-224, TP-20, and $TiO_2$ (Fig. S23). $TiO_2$ hardly produces $H_2O_2$, while PCN-224 and TP-20 produce a small amount of $H_2O_2$. It is speculated that the·OH produced by $TiO_2$ comes from the conversion of $OH^-$, while·OH produced by PCN-224 comes from the oxidation of part $H_2O_2$ by $h^+$. Typically, the production of $O_2^-$ depends on $e^-$, and the tight

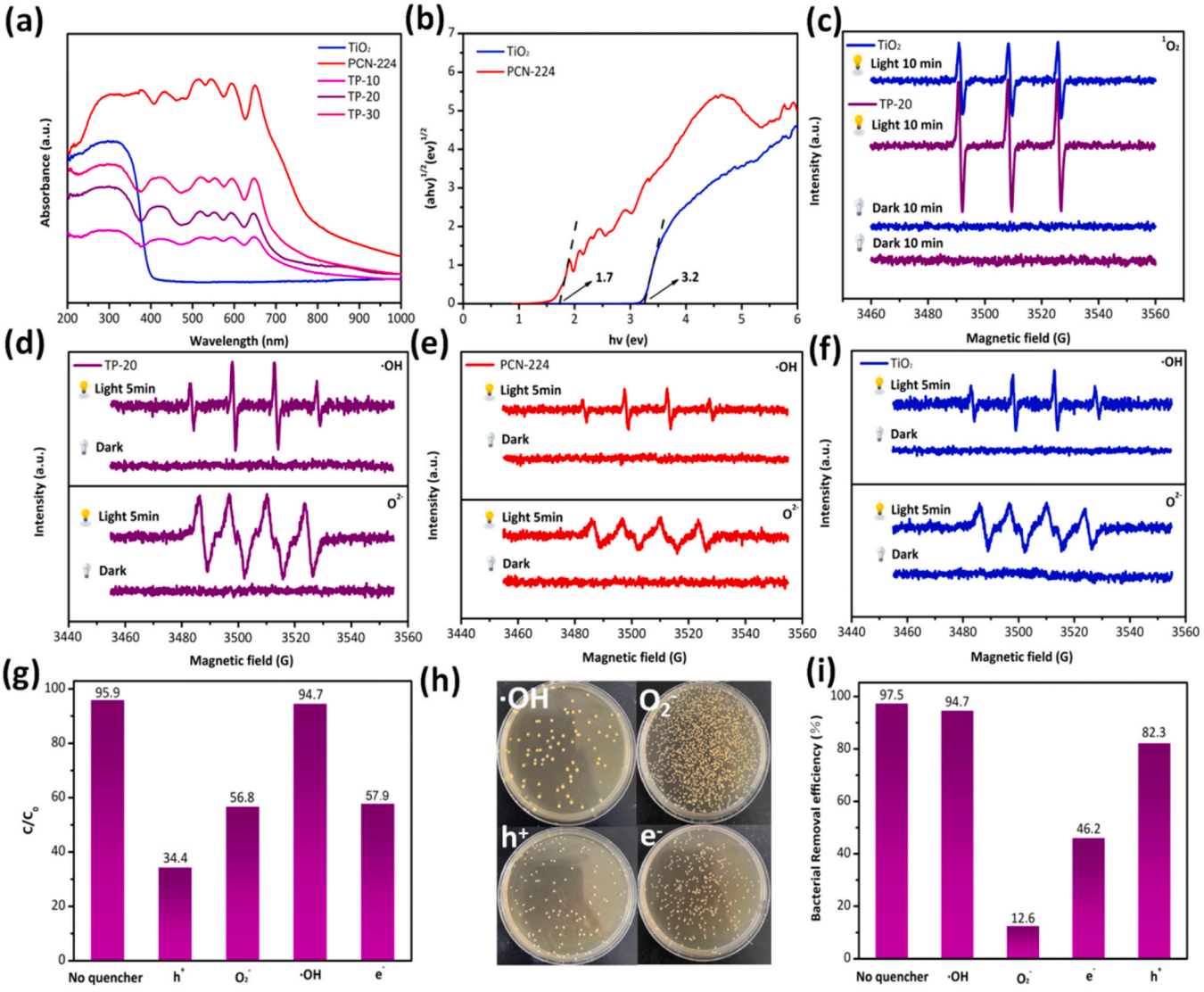


**Fig. 8.** (a) UV–vis spectra, (b) band gap of $TiO_2$ and PCN-224. ESR spectra of $TiO_2$, PCN-224 and TP-20: (c) 2,2,6,6-Tetramethyl-4-piperidinone hydrochloride (TEMP) - $^1O_2$, (d-f) 5,5-dietyl-1-pyrroline-n-oxide (DMPO) - $O_2^-$ and DMPO -·OH. (g) Radicals capturing experiments during TC degradation and (h-i) photocatalytic sterilization of TP-20.

interface between $TiO_2$ and PCN-224 provides a fast channel for $e^-$ transfer, which is the reason for the high production of $O_2^-$ over the TP-20. In addition, the ability of TP-20 to produce $^1O_2$ under light conditions was tested (Fig. 8c). Compared with $TiO_2$, the TP-20 generates more $^1O_2$ radicals, which is attributed to the fact that the generated $O_2^-$ is further oxidized by $h^+$ to form $^1O_2$. Sodium oxalate ($Na_2C_2O_2$), isopropyl alcohol (IPA), 4-hydroxy-2,2,6,6-tetramethyl (TEMPOL) and potassium dichromate ($K_2Cr_2O_7$) were introduced in the reaction process of the TC degradation and inactivation *S. aureus* to achieve the purpose of quenching $h^+$,·OH, $O_2^-$ and $e^-$. It can be found that different radical plays a primary role in the TC degradation and inactivation *S. aureus*. As shown in Fig. 8g, when $Na_2C_2O_2$ is added, the degradation rate only reaches 34.4%, indicating that $h^+$ plays a decisive role in the photocatalytic TC degradation process, while $O_2^-$, $e^-$ and·OH only play a relatively small role. As for the inactivation *S. aureus*, when the $O_2^-$ produced is quenched with TEMPOL, the bactericide efficiency is reduced to 12.6% (Fig. 8i), indicating that the $O_2^-$ radical plays a decisive role. The $O_2^-$ and·OH radicals can work together attack the cell wall, thus causing the break of the cell and protein leakage, resulting in bacterial death. Therefore, for the same catalysts, the functional radical involved in different catalytic reaction may vary for the same TP-20 catalyst. Herein, in the case of TC degradation, the main radical responsible is $h^+$, whereas the $O_2^-$ plays a key role in the inactivation of *S. aureus*.

The photocatalytic mechanism of the TP-20 under visible light has been speculated. It is noted that the $TiO_2$ cannot be excited by visible light; while both of the PCN-224 and TP-20 demonstrate photocatalytic activity, with the TP-20 exhibiting higher activity than PCN-224. This rules out a Type-I transfer mode due to that $e^-$ transit from the CB of $TiO_2$ to the CB of PCN-224 is not possible due to the lack of visible light excitation for $TiO_2$ (Fig. 9). Based on this speculation, in the TP-20 composite, the $TiO_2$ with large amount of empty orbit mainly functions as an electron transfer platform to accelerate the carrier separation. Firstly, PCN-224 generates photogenerated electron-hole pairs; and secondly, $e^-$ at the CB of PCN-224 can further transfer to CB of $TiO_2$, resulting a faster carrier separation. The photocatalytic mechanisms for the $H_2$ generation, TC degradation, and *S. aureus* inactivation of the TP-20 are supposed. In the process of photocatalytic $H_2$ evolution, the $e^-$ on the CB of $TiO_2$ reacts with $H_2O$ to form $H_2$ while the $h^+$ is consumed by the sacrificial agent (TEOA). Photocatalytic sterilization is a relatively complex reaction process, involving multiple ROS. First, the $e^-$ transfers from the CB of PCN-224 to the CB of $TiO_2$ and then reacts with $O_2$ to produce $O_2^-$ radicals; and $h^+$ at PCN-224 also participates in the reaction.

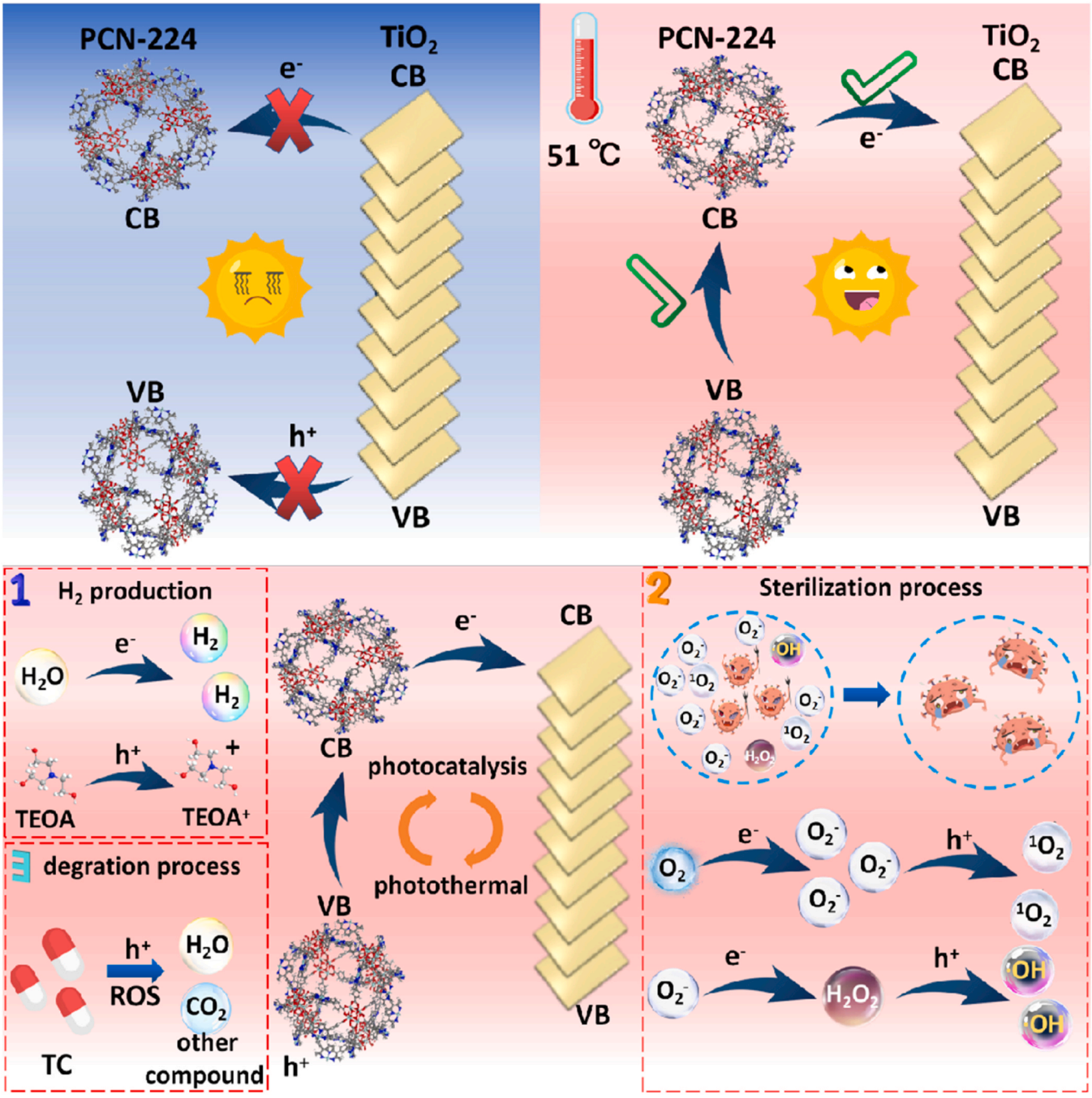


**Fig. 9.** Mechanisms of different photocatalytic reactions on the $TiO_2$/PCN-224 under visible light.

Part of the $O_2^-$ radicals further transform into $^1O_2$ which has strong oxidation capacity can effectively kill the bacterial. Another portion of the $O_2^-$ radicals continues to react with $H_2O$ to form $H_2O_2$ when exposed to $e^-$. The generated $H_2O_2$ decomposes into·OH due to the oxidation of $h^+$ at the VB of PCN-224. However, the photodegradation mechanism of TC on the TP-20 differs from sterilization. It mainly relies on the photogenerated $h^+$ at the VB of PCN-224, which directly oxidize TC into other complexes. The function of acting as an electron transfer platform for $TiO_2$ enables faster carrier separation and generates more radicals, contributing to its high catalytic performance. The photothermal effect generated by the PCN-224 accelerates the reaction kinetics for all three catalytic processes mentioned above. In detail, PCN-224 absorbs light and converts it into heat energy, leading to a high surface temperature of the TP-20 catalyst. This can weaken bacterial tolerance to ROS by increasing the penetrability of bacterial membrane, enhancing the antibacterial activity of the TP-20. Besides that, the photothermal effect generated by the PCN-224 also favors to lower the activation energy of the reactant molecules and promote the charge transfer, thereby improving the efficiency of $H_2$ generation and TC degradation.

## 4. Conclusion

In this work, a visible light responsive $TiO_2$/PCN-224 hybrid based membrane was synthesized for a variety of photocatalytic applications, including $H_2$ generation, TC degradation, and *S. aureus* inactivation. The incorporation of PCN-224 with its photodynamic and photothermal effect, along with the role of $TiO_2$ as the electron transfer platform, resulted in the enhanced migration of photogenerated carriers under

visible light irradiation. This led to the production of miscellaneous radicals ($e^-$, $h^+$, $O_2^-$, and·OH, $^1O_2$) that contributed to the different photocatalytic reactions. Specifically, $e^-$, $h^+$ and $O_2^-$ were found to be the main functional radicals for $H_2$ generation, TC degradation, and *S.aureus* inactivation, respectively. The highly hydrophilic nature of the membrane facilitated the kinetics of water-based reactions and allowed for effective separation and recycling. Under visible light conditions, the TP-20 hybrid membrane exhibited effectiveness for $H_2$ generation (1.88 mmol $g^{-1}$ $h^{-1}$), and TC degradation (86%, 120 min) and *S. aureus* inactivation (99.99%, 120 min), respectively, achieving the goal of "three birds, one stone." Under Xe lamp light, both of the PCN-224 and $TiO_2$ can be excited to provide double excitation modes, the TP-20 hybrid membrane demonstrated even higher performance with $H_2$ evolution of 590.3 μmol $g^{-1}$ $h^{-1}$, TC degradation of 96% (90 min), and *S. aureus* inactivation of 99.99% (90 min). This research not only enriches knowledge and experience for future work but also paves the way for future investigations on multifunctional photocatalytic materials.

## CRediT authorship contribution statement

**Zhongxi Lu:** Experiments, Investigation, Writing – original draft, Visualization. **Jingsong Gao:** Investigation, Writing – original draft. **Shaosheng Rao:** Conceptualization, Writing – review & editing. **Cheng Jin:** Writing – review & editing. **Haopeng Jiang:** Investigation. **Jun Shen:** Writing – review & editing, **Xiaohui Yu:** Investigation. **Weikang Wang:** Experimental method. **Lele Wang:** Experimental method. **Juan Yang:** Experimental method. **Qinqin Liu:** Supervision, Project administration, Funding acquisition.

## Declaration of Competing Interest

The authors declare that they have no known competing financial interests or personal relationships that could have appeared to influence the work reported in this paper.

## Data availability

No data was used for the research described in the article.

## Acknowledgements

This work was supported by Natural Science Foundation of China (21972058, 22102064). This work sponsored by Qing Lan Project of Jiangsu Province (2022).

## Appendix A. Supporting information

Supplementary data associated with this article can be found in the online version at doi:10.1016/j.apcatb.2023.123374.

## References

[1] J. Cheng, S. Wan, S. Cao, Promoting solar-driven hydrogen peroxide production over thiazole-based conjugated polymers via generating and converting singlet oxygen, Angew. Chem. Int. Ed. (2023), 202310476.
[2] H. Huang, R. Shi, Z. Li, J. Zhao, C. Su, T. Zhang, Triphase photocatalytic $CO_2$ reduction over silver-decorated titanium oxide at a gas–water boundary, Angew. Chem. Int. Ed. 61 (2022), 202200802.
[3] F. Zhang, Y. Zhu, Q. Lin, L. Zhang, X. Zhang, H. Wang, Noble-metal single-atoms in thermocatalysis, electrocatalysis, and photocatalysis, Energy Environ. Sci. 14 (2021) 2954–3009.
[4] H. Sun, K. Xiao, Y. Ma, S. Xiao, Q. Zhang, C. Su, P. Wong, Vacancy-rich $BiO_{2-x}$ as a highly-efficient persulfate activator under near infrared irradiation for bacterial inactivation and mechanism study, J. Hazard. Mater. 431 (2022), 128510.
[5] P. Robertson, J. Roberston, D. Bahnemann, Removal of microorganisms and their chemical metabolites from water using semiconductor photocatalysis, J. Hazard. Mater. 211–212 (2012) 161–171.
[6] M. Kou, Y. Wang, Y. Xu, L. Ye, Y. Huang, B. Jia, H. Li, J. Ren, Y. Deng, J. Chen, Y. Zhou, K. Lei, L. Wang, W. Liu, H. Huang, T. Ma, Molecularly engineered covalent organic frameworks for hydrogen peroxide photosynthesis, Angew. Chem. Int. Ed. 61 (2022), 202200413.
[7] P. Xia, S. Cao, B. Zhu, M. Liu, M. Shi, J. Yu, Y. Zhang, Designing a 0D/2D S-scheme heterojunction over polymeric carbon nitride for visible-light photocatalytic inactivation of bacteria, Angew. Chem. Int. Ed. 59 (2020) 5218–5225.
[8] B. Cowie, V. Porley, N. Robertson, Solar disinfection (SODIS) provides a much underexploited opportunity for researchers in photocatalytic water treatment (PWT), ACS Catal. 10 (2020) 11779–11782.
[9] A. Fujishima, K. Honda, Electrochemical photolysis of water at a semiconductor electrode, Nature 238 (1972) 37–38.
[10] L. Wang, T. Yang, L. Peng, Q. Zhang, X. She, H. Tang, Q. Liu, Dual transfer channels of photo-carriers in 2D/2D/2D sandwich-like $ZnIn_2S_4$/g-$C_3N_4$/$Ti_3C_2$ MXene S-scheme/Schottky heterojunction for boosting photocatalytic $H_2$ evolution, Chin. J. Catal. 43 (2022) 2720–2731.
[11] X. Yu, H. Su, J. Zou, Q. Liu, L. Wang, H. Tang, Doping-induced metal-N active sites and bandgap engineering in graphitic carbon nitride for enhancing photocatalytic $H_2$ evolution performance, Chin. J. Catal. 43 (2022) 421–432.
[12] Y. Zhao, Y. Wang, X. Liang, H. Shi, C. Wang, J. Fan, X. Hu, E. Liu, Enhanced photocatalytic activity of Ag-$CsPbBr_3$/CN composite for broad spectrum photocatalytic degradation of cephalosporin antibiotics 7-ACA, Appl. Catal. B Environ. 247 (2019) 57–69.
[13] J. Zhou, J. Ding, H. Wan, G. Guan, Boosting photocatalytic degradation of antibiotic wastewater by synergy effect of heterojunction and phosphorus doping, J. Colloid Interface Sci. 582 (2021) 961–968.
[14] J. Gao, S. Rao, X. Yu, L. Wang, J. Xu, J. Yang, Q. Liu, Dimensional-matched two dimensional/two dimensional $TiO_2$/$Bi_2O_3$ step-scheme heterojunction for boosted photocatalytic performance of sterilization and water splitting, J. Colloid Inter. Sci. 628 (2022) 166–178.
[15] C. Jin, D. Sun, Z. Sun, S. Rao, Z. Wu, C. Cheng, L. Liu, Q. Liu, J. Yang, Interfacial engineering of Ni-phytate and $Ti_3C_2T_x$ MXene-sensitized $TiO_2$ toward enhanced sterilization efficacy under 808 nm NIR light irradiation, Appl. Catal. B Environ. 330 (2023), 122613.
[16] H. Jiang, W. Wang, L. Sun, T. Kong, Z. Lu, H. Tang, L. Wang, Q. Liu, Boosting photocatalytic $CO_2$ reduction by tuning photogenerated carrier kinetics in two-dimensional $WO_x$/BiOCl S-scheme heterojunction with oxygen vacancies, J. Catal. 416 (2022) 1–10.
[17] H. Jiang, L. Wang, X. Yu, L. Sun, J. Li, J. Yang, Q. Liu, Precise regulation of built-in electric field over $NH_2$-MIL-125-Ti/$WO_{3-x}$ S-scheme heterojunction for achieving simultaneous formation of CO and $H_2O_2$ from $CO_2$ and $H_2O$, Chem. Eng. J. 466 (2023), 143129.
[18] Q. Guo, C. Zhou, Z. Ma, X. Yang, Fundamentals of $TiO_2$ photocatalysis: concepts, mechanisms, and challenges, Adv. Mater. 31 (2019) 1901997.
[19] L. Liccardo, M. Bordin, P. Sheverdyaeva, M. Belli, P. Moras, A. Vomiero, E. Moretti, Surface defect engineering in colored $TiO_2$ hollow spheres toward efficient photocatalysis, Adv. Funct. Mater. 33 (2023) 2212486.
[20] J. Yang, L. Chen, W. Tan, B. Han, Y. Xu, W. Wang, J. Xu, Y. Wang, MIL-125(Ti)-derived double vacancy-induced enhanced visible-light-driven $TiO_2$ p-n homojunction for photocatalytic elimination of OFL and Cr(VI), J. Environ. Chem. Eng. 11 (2023), 109721.
[21] E. Musa, S. Kaur, T. Gallagher, T. Anthony, W. Stickle, L. Arnadottir, K. Stylianou, Two Birds, One Stone: coupling hydrogen production with herbicide degradation over metal-organic framework-derived titanium dioxide, ACS Catal. 13 (2023) 3710–3722.
[22] J. Zhang, C. Toe, P. Kumar, J. Scott, R. Amal, Engineering defects in $TiO_2$ for the simultaneous production of hydrogen and organic products, Appl. Catal. B Environ. 333 (2023), 122765.
[23] A. Meng, L. Zhang, B. Cheng, J. Yu, Dual cocatalysts in $TiO_2$ photocatalysis, Adv. Mater. 31 (2019) 1807660.
[24] Q. Guo, Z. Ma, C. Zhou, Z. Ren, X. Yang, Single molecule photocatalysis on $TiO_2$ surfaces, Chem. Rev. 119 (2019) 11020–11041.
[25] L. Wang, G. Tang, S. Liu, H. Dong, Q. Liu, J. Sun, H. Tang, Interfacial active-site-rich 0D $Co_3O_4$/1D $TiO_2$ p-n heterojunction for enhanced photocatalytic hydrogen evolution, Chem. Eng. J. 428 (2022), 131338.
[26] C. Zhu, H. Yao, S. Le, Y. Yin, C. Chen, H. Xu, S. Wang, X. Duan, S-scheme photocatalysis induced by ultrathin $TiO_2$(B) nanosheets-anchored hierarchical $In_2S_3$ spheres for boosted photocatalytic activity, Compos. Part B Eng. 242 (2022), 110082.
[27] X. Li, J. Shi, H. Hao, X. Lang, Visible light-induced selective oxidation of alcohols with air by dye-sensitized $TiO_2$ photocatalysis, Appl. Catal. B Environ. 232 (2018) 260–267.
[28] Z. Wang, X. Lang, Visible light photocatalysis of dye-sensitized $TiO_2$: The selective aerobic oxidation of amines to imines, Appl. Catal. B Environ. 224 (2018) 404–409.
[29] Y. Pi, X. Li, Q. Xia, J. Wu, Y. Li, J. Xiao, Z. Li, Adsorptive and photocatalytic removal of persistent organic pollutants (POPs) in water by metal-organic frameworks (MOFs), Chem. Eng. J. 337 (2018) 351–371.
[30] J. Liang, H. Yu, J. Shi, B. Li, L. Wu, M. Wang, Dislocated bilayer MOF enables high-selectivity photocatalytic reduction of $CO_2$ to CO, Adv. Mater. 35 (2023), 220814.
[31] F. Yang, W. Yu, Q. Yu, X. Liu, C. Liu, C. Lu, X. Liao, Y. Liu, N. Peng, Mitochondria-targeted nanosystem with reactive oxygen species-controlled release of CO to enhance photodynamic therapy of PCN-224 by sensitizing ferroptosis, Small 19 (2023) 2206124.
[32] M. Chen, Z. Long, R. Dong, L. Wang, J. Zhang, S. Li, X. Zhao, X. Hou, H. Shao, X. Jiang, Titanium incorporation into Zr-porphyrinic metal-organic frameworks with enhanced antibacterial activity against multidrug-resistant pathogens, Small 16 (2020) 1906240.

[33] S. Xu, Y. Lin, X. Zhao, Z. Liang, Y. Hu, Z. Chen, X. Ren, X. Mei, NIR triggered photocatalytic and photothermal bifunctional MOF nanozyme using for improving osteoarthritis microenvironment by repairing injured chondrocytes of mitochondria, Chem. Eng. J. 468 (2023), 143826.
[34] X. Nie, S. Wu, S. Liao, J. Chen, F. Huang, W. Li, Q. Wang, Q. Wei, Light-driven self-disinfecting textiles functionalized by PCN-224 and Ag nanoparticles, J. Hazard. Mater. 416 (2021), 125786.
[35] Y. Luo, X. Liu, L. Tan, Z. Li, K. Yeung, Y. Zheng, Z. Cui, Y. Liang, S. Zhu, C. Li, X. Wang, S. Wu, Enhanced photocatalytic and photothermal properties of ecofriendly metalorganic framework heterojunction for rapid sterilization, Chem. Eng. J. 405 (2021), 126730.
[36] H. Zhang, Y. Wan, J. Luo, S. Darling, Drawing on membrane photocatalysis for fouling mitigation, ACS Appl. Mater. Interfaces 13 (2021) 14844–14865.
[37] Z. Li, Z. Sun, G. Zhang, Combining heterogeneous photocatalysis and enzymatic catalysis via membrane: Conversion of biomass for $H_2$ production from water, Appl. Catal. B Environ. 338 (2023), 123069.
[38] L. Li, C. Luo, X. Chen, N. Chu, L. Li, M. Chao, L. Yan, A novel multifunctional photocatalytic separation membrane based on single-component seaweed-like g-$C_3N_4$, Adv. Funct. Mater. 33 (2023) 2213974.
[39] F. Chen, Y. Li, M. Zhou, X. Gong, Y. Gao, G. Cheng, S. Ren, D. Han, Smart multifunctional direct Z-scheme $In_2S_3$@PCN-224 heterojunction for simultaneous detection and photodegradation towards antibiotic pollutants, Appl. Catal. B Environ. 328 (2023), 122517.
[40] Y. Lu, W. Yin, K. Peng, K. Wang, Q. Hu, A. Selloni, F. Chen, L. Liu, M. Sui, Self-hydrogenated shell promoting photocatalytic $H_2$ evolution on anatase $TiO_2$, Nat. Commun. 9 (2018) 2752.
[41] P. Jin, L. Wang, X. Ma, R. Lian, J. Huang, H. She, M. Zhang, Q. Wang, Construction of hierarchical $ZnIn_2S_4$@PCN-224 heterojunction for boosting photocatalytic performance in hydrogen production and degradation of tetracycline hydrochloride, Appl. Catal. B Environ. 284 (2021), 119762.
[42] Y. Zhao, M. Yuan, H. Yang, J. Li, Y. Ying, J. Li, W. Wang, S. Wang, Versatile multi-wavelength light-responsive metal-organic frameworks micromotor through porphyrin metalation for water sterilization, Small (2023) 2305189.
[43] L. Wang, Y. Liu, J. Hao, Z. Ma, Y. Lu, M. Zhang, C. Hou, Construction of an S-scheme $TiOF_2$/$HTiOF_3$ heterostructures with abundant OVs and O-H groups: Performance, kinetics and mechanism insight, J. Colloid Interface Sci. 640 (2023) 15–30.
[44] H. Bui, D. Thuan, P. Huong, K. Nguyen, M. Nguyen, T. Chu, Q. Le, K. Jitae, S. Devanesan, M. Alsalhi, T. Nguyen, Enhanced photocatalytic $H_2$ evolution and photodegradation of antibiotic tetracycline in wastewater by $TiO_2$@$Ti_3C_2$, Int. J. Hydrogen Energy, ⟨https://doi.org/10.1016/j.ijhydene.2022.07.128⟩.
[45] X. Dai, S. Feng, W. Wu, Y. Zhou, Z. Ye, X. Cao, Y. Wang, C. Yang, Photocatalytic hydrogen evolution and antibiotic degradation by S-scheme $ZnCo_2S_4$/$TiO_2$, Int. J. Hydrog. Energy 47 (2022) 25104–25116.
[46] J. Guo, W. Gan, C. Ding, Y. Lu, J. Li, S. Qi, M. Zhang, Z. Qi, Black phosphorus quantum dots and Ag nanoparticles co-modified $TiO_2$ nanorod arrays as powerful photocatalyst for tetracycline hydrochloride degradation: Pathways, toxicity assessment, and mechanism insight, Sep. Purif. Technol. 297 (2022), 121454.
[47] K. Sekar, C. Chuaicham, B. Vellaichamy, W. Li, W. Z, X. Lu, B. Ohtani, K. Sasaki, Cubic $Cu_2O$ nanoparticles decorated on $TiO_2$ nanofiber heterostructure as an excellent synergistic photocatalyst for $H_2$ production and sulfamethoxazole degradation, Appl. Catal. B Environ. 294 (2021), 120221.
[48] C. Wu, J. Dai, J. Ma, T. Zhang, L. Qiang, J. Xue, Mechanistic study of B-$TiO_2$/$BiVO_4$ S-scheme heterojunction photocatalyst for tetracycline hydrochloride removal and $H_2$ production, Sep. Purif. Technol. 312 (2023), 123398.
[49] B. Zhang, J. Zhang, X. Tan, D. Shao, J. Shi, L. Zheng, J. Zhang, G. Yang, B. Han, MIL-125-$NH_2$@$TiO_2$ core-shell particles produced by a post-solvothermal route for high-performance photocatalytic $H_2$ production, ACS Appl. Mater. Interfaces 10 (2018) 16418–16423.
[50] Y. Wang, J. Li, Q. Hu, M. Hao, Y. Liu, L. Gong, R. Li, X. Huang, Boosting visible-light-driven photocatalytic hydrogen production through sensitizing $TiO_2$ via novel nanoclusters, ACS Appl. Mater. Interfaces 13 (2021) 40562–40570.
[51] K. Ma, M. Zhang, W. Sun, C. Dong, Y. Dong, W. Hao, Y. Ding, Revealing different depth boron substitution on interfacial charge transfer in $TiO_2$ for enhanced visible-light $H_2$ production, Appl. Catal. B Environ. 315 (2022), 121570.
[52] H. Li, B. Sun, T. Gao, H. Li, Y. Ren, G. Zhou, $Ti_3C_2$ MXene co-catalyst assembled with mesoporous $TiO_2$ for boosting photocatalytic activity of methyl orange degradation and hydrogen production, Chin. J. Catal. 43 (2022) 461–471.
[53] B. Zhu, X. Hong, L. Tang, Q. Liu, H. Tang, Enhanced photocatalytic $CO_2$ reduction over 2D/1D $BiOBr_{0.5}Cl_{0.5}$/$WO_3$ S-scheme heterostructure, Acta Phys. -Chim. Sin. 38 (2022) 2111008.